Sensors and Actuators A 148 (2008) 138–148

Contents lists available at ScienceDirect

Sensors and Actuators A: Physical

journal homepage: www.elsevier.com/locate/sna

Evaluation of the performance of a valveless micropump by CFD and lumped-system analyses

Yeng-Yung Tsui*, Shiue-Lin Lu

Department of Mechanical Engineering, National Chiao Tung University, Hsinchu 300, Taiwan, ROC

ARTICLE INFO

Article history:
Received 18 March 2008
Received in revised form 29 June 2008
Accepted 30 June 2008
Available online 15 July 2008

Keywords:
Valveless micropumps
Nozzle/diffuser
Lumped-system analysis
CFD analysis

ABSTRACT

The flow in a valveless micropump is analyzed using both the CFD method and the lumped-system method. In the multidimensional simulation of the CFD model, the Navier–Stokes equations are solved using a finite volume method suitable for the use of unstructured grids. The moving membrane is modeled by imposing a reciprocating velocity boundary condition. It is seen that a good agreement with measurements can be obtained for various back pressures by adopting an appropriate membrane shape blending the parabolic and the trapezoidal profiles. The multidimensional predictions serve as benchmark solutions to the lumped-system analysis. In the latter analysis two correlations for the loss coefficients of the nozzle and the diffuser are employed. The results show that with a more accurate one of the two correlations, a better agreement with the multidimensional calculations is yielded. The performance of the pump can be evaluated by considering the pumping efficiency. The pumping efficiency can be approximately formulated in two different ways, depending on the average ratios of the outlet flow rate to the inlet flow rate in the pumping and supply stages. In the averaging process to determine the mean ratios, the transient region between the pumping stage and the supply stage is excluded. This leads to even closer agreement to the multidimensional calculations in the pumping efficiency.

1. Introduction

Microfluidic systems are of interest in medical testing, drug delivery, chemical analysis, chip cooling and many others. Microsystems have the advantages of small volume, cheap cost, high precision and fast reaction time. Micropumps are essential devices in the microfluidic systems, which provide momentum to cause fluid flow. The development of micropumps has been based on various principles [1–3]. They can be divided into two categories: mechanical and non-mechanical [1]. Most mechanical pumps use oscillatory movement of mechanical parts to drive the flow. Some examples include check valve micropumps, peristaltic micropumps and rotary micropumps. In the non-mechanical category, the cause of fluid flow is mainly via electric–fluid interactions, such us electrokinetic micropumps, electrohydrodynamic micropumps, etc.

In general, mechanical micropumps have higher flow rates than the non-mechanical micropumps. Among the various mechanical micropumps the valveless membrane micropumps have drawn much attention in recent years. The actuation of the reciprocating membrane can be achieved by different ways, such as piezoelectric discs, pneumatic actuators, thermomechanic actuators, to name a few. Most of the membrane micropumps are constructed with intake and exhaust valves to direct the fluid flow. During miniaturization of these pumps, the presence of the moving valves leads to manufacturing difficulties and suffers the risk of wear and fatigue. Furthermore, if particles are present in the pumps, there is a concern about valve clogging. To avoid these drawbacks, a novel idea is to replace the moving valves with fluidic diodes, such as nozzle/diffuser elements or the valvular conduits. Fluidic diodes have different flow resistances when the direction of the flow through the devices is reversed. In the positive direction through a diffuser the velocity is reduced and static pressure is gradually recovered. As the fluid flows in the reversed direction, the device functions as a nozzle and larger loss is caused. Thus, for a reciprocating flow through such a device, it performs the function of directing a net flow in the positive direction. Incorporation of the nozzle/diffuser elements into micropumps was realized first by Stemme and Stemme [4] and then by Gerlach and Wurmus [5]. Olsson et al. [6] described a flat, planar design with the nozzle/diffuser arranged in the same plane as the pump chamber. This kind of planar micropumps can be fabricated using a commercially available injection-molding machine for compact disc manufacture [7]. This means that it can be produced in high volumes at low costs.

A simple way to analyze the flow in valveless micropumps is the use of the lumped-system method. This approach ignores spatial variation and focuses mainly on the time variation. Ullmann

* Corresponding author. Tel.: +886 3 5131556; fax: +886 3 5720634.
E-mail address: yytsui@mail.nctu.edu.tw (Y.-Y. Tsui).

0924-4247/$ – see front matter © 2008 Elsevier B.V. All rights reserved.
doi:10.1016/j.sna.2008.06.036

Nomenclature

A_L, A_t	areas of the two ends of the nozzle/diffuser
f	oscillating frequency
F^c, F^d	convective and diffusive fluxes
h	deflection of the membrane
K	loss coefficient
K_d, K_n	loss coefficients of the diffuser and the nozzle
$\dot{m}$	mass flux
P	pressure
P_c	pressure in the chamber
P_{in}, P_{out}	pressures at the inlet and the outlet
Q	volumetric flow rate
Q_1, Q_2	volumetric flow rates at the inlet and the outlet
r	radial distance
r_o	radius of the pump chamber
r_l	radius of the piezo disc
$\vec{S}_f$	surface vector of considered face
t	time
T	one oscillating period
V_m	half the maximum volume swept by the membrane
w	weighting factor
W	oscillating velocity of the membrane
Z	time-dependent variation of the deflection of the membrane

Greek symbols

β	ratio of Q_2 to Q_1
δ_{pc}	distance vector connecting the principal node p and the neighboring node c
η	pumping efficiency
η_R	real efficiency
η_1, η_2, η_3	approximate efficiencies
μ	fluid viscosity
ρ	fluid density

Subscripts

c	chamber
d	diffuser
en	entrance
ex	exit
in	inlet
max	maximum value
n	nozzle
out	outlet
p	pumping stage or parabolic profile
s	supply stage
t	trapezoidal profile

Superscripts

t	total value

[8] proposed a simple model based on the principle of mass conservation over the pump chamber. With this method a variety of single-chamber and double-chamber micropumps were analyzed to find the flow output rate. In the lump model of Olsson et al. [9], the conservation of both the mass and energy was considered. A sub-model, based on momentum balance over the membrane, was included to account for the interaction between the membrane and the fluid flow. In the study of Pan et al. [10], the movement of the membrane was modeled by a partial differential equation taken from the clamped-thin-plate theory. The equations were approximately solved by the small parameter perturbation method and the Galerkin method. However, the flow unsteadiness within the micropump was not taken into account. Pan et al. [11] showed that this inertial force is not negligible, compared with the viscous loss, in the dynamic coupling analysis.

The recent development of Navier–Stokes equations solvers has made three-dimensional calculations possible in complicated geometry. This multidimensional analysis approach can provide accurate solutions as well as detailed flow field. Nguyen and Huang [12] reported a numerical simulation of pulse-width-modulated micropumps with nozzle/diffuser elements. The vibration of the membrane was modeled by either a moving wall or moving velocities as the boundary condition. In both models, the interaction between the structure analysis and flow analysis is neglected. Yang et al. [13] evaluated the performance of micropumps with two chambers arranged in parallel or series combination. In the series arrangement with 90° phase angle difference between the two membranes, an eightfold increase of flow rate was yielded, relative to the single-chamber pump. A study of complete coupling between the electrical, mechanical and fluid systems in a piezoelectric-actuated micropumps was conducted by Fan et al. [14] using finite element method and computational fluid dynamics. The behavior of the membrane at different frequencies, which may affect the pumping rate, was investigated. It was found that the pumping rate as well as the deflection amplitude of the membrane increases with the increasing frequency of the vibrating membrane for frequencies less than 7.5 kHz. Further increase of frequency leads to degradation of pumping rate due to the undesirable deflection way of the membrane. The fluid–structure interaction and the electro-mechanical coupling were also employed in the studies by Yao et al. [15] and Jeong and Kim [16].

It could be found from the above numerical studies that most CFD simulations were performed using commercial codes, especially the CFD-ACE. Recently, a computational procedure based on the use of the fully conservative finite volume method and the unstructured mesh was developed for both compressible and incompressible flows by the group of the present authors [17,18]. In order to analyze the periodic flow encountered in micropumps, this method is modified to cope with the unsteady state. In addition, a way to implement the pressure boundary condition, easily applicable to unstructured grids, is addressed. A lumped-system analysis is also conducted. The lump model is assessed by comparing with the results obtained from multidimensional calculations.

2. Multidimensional method

A drawing of the micropump under consideration is shown in Fig. 1. Only half of the pump is considered in calculations due to its symmetric geometry. The membrane is placed on the top of the main chamber with a diameter of 6 mm. A piezo disc of diameter 4 mm is attached to cause vibration of the membrane. The opening on the left chamber is the inlet and that on the right chamber the outlet. Both openings have a diameter 1 mm. Nozzle/diffuser elements are used to connect the inlet and the outlet chambers on both sides of the main chamber. The length of this element is 1 mm with a diffusion angle of 7° and the width at the throat is 0.1 mm. The height of the micropump is 0.2 mm.

The dynamics of the flow in the micropump is modeled by the incompressible Navier–Stokes equations which can be cast into the following form:

$$\frac{\partial \rho\phi}{\partial t} + \nabla \cdot (\rho \vec{V}\phi) = \mu \nabla^2 \phi + S \quad (1)$$

where ϕ represents Cartesian velocity components and the source S includes the pressure gradients. Integrating the equation over a control volume, which can be of arbitrary geometry, and using the

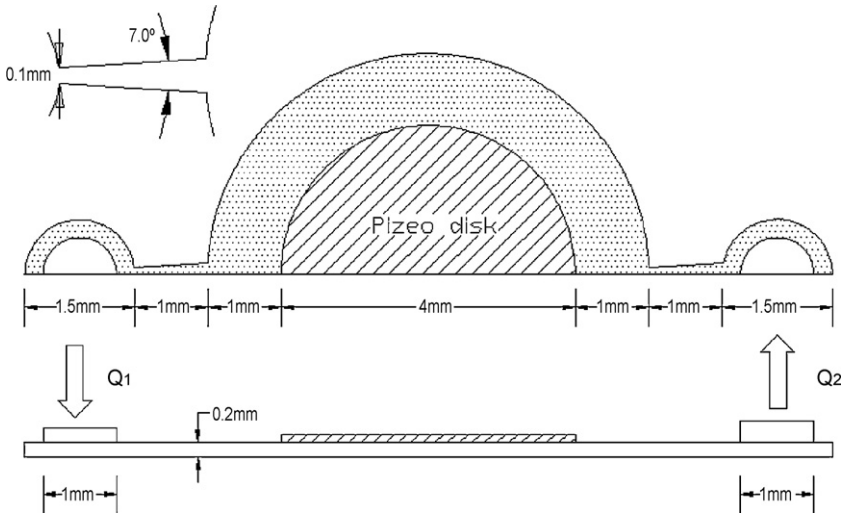

Fig. 1. Configuration of the valveless micropump.

divergence theorem lead to:

$$\frac{\rho\,\Delta V}{\Delta t}(\phi-\phi^{o})+\int_s \rho\phi\vec{V}\cdot \mathrm{d}\vec{S}=\mu\int_s \nabla\phi\cdot \mathrm{d}\vec{S}+S\;\Delta V \tag{2}$$

where ΔV is the volume of the considered cell, ϕ^{o} denotes the velocity component at old time step. Here the fully implicit scheme is used for the time discretization. The convection and diffusion terms have been transformed into a surface integral form by the divergence theorem. The convective flux through the surface of the control volume can be approximated by

$$F^{c}=\sum \rho(\vec{V}\cdot\vec{S})_{f}\phi_{f} \tag{3}$$

where the subscripts f stand for face values, $\vec{S}_f$ is the surface vector, and the summation is taken over all the faces of the control volume surface. The face value ϕ_f is approximated using a scheme blending the upwind and the central differences with a weighting factor of 0.9 biased toward the central difference. The diffusive flux is approximated by

$$F^{d}=\sum\left[\frac{\mu S_f^2}{\vec{\delta}_{pc}\cdot\vec{S}_f}(\phi_c-\phi_p)+\mu\overline{\nabla\phi}_f\left(\vec{S}_f-\frac{S_f^2}{\vec{\delta}_{pc}\cdot\vec{S}_f}\vec{\delta}_{pc}\right)\right] \tag{4}$$

The subscripts p and c denote the centroids of the principal cell and the neighboring cell on the two sides adjacent to the face f, $\vec{\delta}_{pc}$ is the distance vector directed from node p to node c (see Fig. 2) $\overline{\nabla\phi}_f$ represents the gradient at the face obtained by linear interpolation from the two nodes p and c.

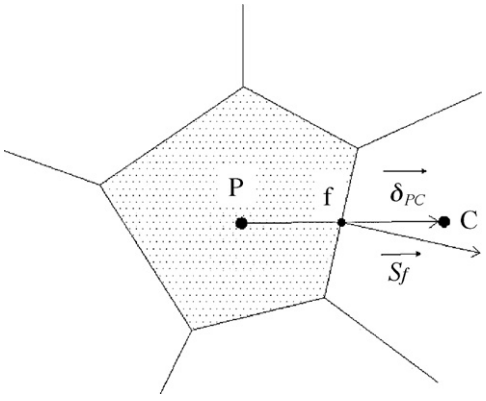

Fig. 2. Illustration of a typical control volume with neighboring cells.

The coupling between the momentum and the continuity equations is treated in a manner similar to the SIMPLE algorithm. The velocities and pressure are collocated on the centroid of each control volume. To avoid checkerboard oscillations resulting from the decoupling between the velocity and the pressure, the momentum interpolation method is adopted. Details about the discretization and the method can be found in the studies [17,18]. However, for unsteady flow the use of SIMPLE algorithm requires iteration in each time step, which is time consuming. Therefore, the non-iterative, predictor–corrector procedure of PISO algorithm [19] is employed. In the predictor step, the momentum equation is solved using the prevailing pressure field. It is followed by a corrector step in which the velocity and pressure are adjusted such that the mass is conserved. Although the new velocity field after the first corrector step satisfies the continuity constraint, the momentum equation is not adequately solved. The PISO algorithm relies on a second corrector to make the pressure field get rid of the mass imbalance left by the predictor step and give letter approximation to the momentum conservation. It is this step to make the PISO different from the SIMPLE and result in higher computational efficiency even in steady flow calculations.

For the micropump under investigation, appropriate boundary conditions must be imposed on both the membrane and the inlet and outlet. It is usual to specify a pressure difference across the inlet and the outlet and the flow rate through these boundaries are sought. To determine the mass flux, or the velocity, at an open boundary with a specified pressure, one approach is to make an approximation to the momentum equation in a manner similar to that used at an internal face. Although this method has been successfully implemented in steady flow calculations [20,21], it may not be appropriate in the non-iterative procedure of the PISO algorithm because the mass is not conserved. In the following, a method, ensuring conservation of mass, is described. Fig. 3 illustrates a control volume P next to an open boundary. The boundary pressure P_b is prescribed at the centroid of this cell. As usually done for non-staggered grid calculations, an extrapolation practice is undertaken to find the pressure on the boundary node B. With this boundary face pressure, the velocity at the node P can be solved for in the momentum predictor step in the same way as the other internal nodes. After the mass fluxes through all the internal faces are calculated using the momentum interpolation method mentioned above, the mass flux through the open boundary $\dot{m}_b$ is then obtained via conservation of mass in this boundary

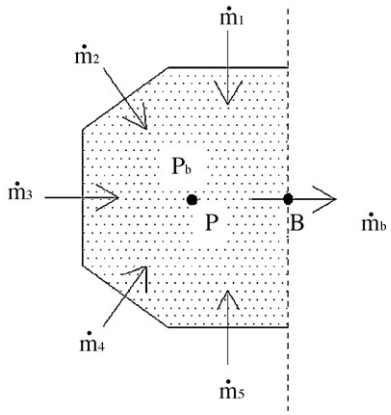

Fig. 3. Illustration of implementation of the pressure condition at a boundary cell.

cell.

$$\dot{m}_b + \sum \dot{m}_i = 0 \tag{5}$$

where $\dot{m}_i$ denotes the mass flux through an internal face and the summation is taken over all the internal faces.

Since the main concern of this study is the fluid flow in the pump, the interaction between the fluid and the structure is neglected. The deflection of the membrane can be modeled by prescribed shapes. The plate-and-shell theory of Timoshenko and Woinowsky-Krieger [22] leads to a fourth-order polynomial for the deflection of a clamped circular plate with uniformly distributed load. The fluid–structure interaction calculations by Jeong and Kim [16] showed that the displacement of the piezoelectric membrane varies in a trapezoidal-like profile. In the present study, the deflection of the membrane is modeled by a combination of two profiles. One is of parabolic profile:

$$h_p(r) = h_{max}\left(1 - \frac{r^2}{r_o^2}\right) \tag{6}$$

The other is of trapezoidal profile:

$$h_t(r) = h_{max} \cdot \text{Max}\left(1, \frac{r_o - r}{r_o - r_1}\right) \tag{7}$$

Here h_{max} is the maximum deflection of the membrane at the center, r_o the radius of the pump chamber, r_1 the radius of the piezo disc, and r is the coordinate in the radial direction. These two profiles are combined in a linear manner:

$$h(r) = (1 - w)h_p(r) + wh_t(r) \tag{8}$$

where w is a weighting factor. The determination of the weighting factor depends on the pressure difference between the inlet and the outlet, which will be given later in Section 5. Because of the small membrane deflection (h_{max} = 1 μm) compared with the chamber height (0.2 mm), the influence of the variation of the pump chamber can be ignored. Instead of the moving wall boundary condition, a velocity in harmonic motion is imposed on the membrane which is assumed to be fixed at its neutral position. The time-dependent variation of the deflection is given by

$$Z(r, t) = -h(r)\ \cos(2\pi f \cdot t) \tag{9}$$

The oscillating velocity is then obtained as

$$W(r, t) = 2\pi f \cdot h(r) \cdot \sin(2\pi f \cdot t) \tag{10}$$

Here f is the frequency of the harmonic motion.

The flow in the pump is assumed to be stagnant initially. Calculations proceed until the variation of the flow becomes periodic.

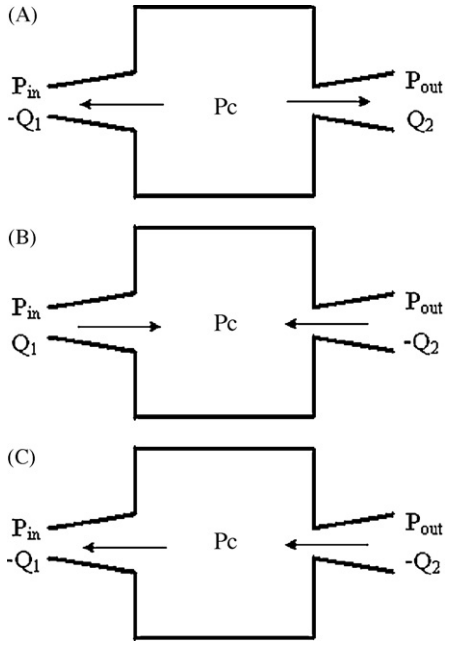

Fig. 4. Illustration of the three modes for the valveless pump. (A) Pump mode: $P_{in} < P_{out} < P_c$; (B) supply mode: $P_c < P_{in} < P_{out}$; (C) transition: $P_{in} < P_c < P_{out}$.

It will be seen that at least three periods are required to reach the fully periodic state.

3. Lumped-system method

As shown in Fig. 4, the pumping process is divided into three modes: pump mode ($P_{in} < P_{out} < P_c$), supply mode ($P_c < P_{in} < P_{out}$), and transition mode ($P_{in} < P_c < P_{out}$). Here P_c is the chamber pressure, P_{in} the inlet pressure, and P_{out} is the outlet pressure. The inlet pressure P_{in} is always smaller than the outlet pressure P_{out}. The volumetric flux through a nozzle/diffuser element is related to the pressure difference across this element by

$$\Delta P = \frac{\rho}{2{A_t}^2} K Q^2 \tag{11}$$

where K is the loss coefficient and A_t is the cross-sectional area at the throat. With the mass conservation over the chamber, the equations governing the three modes can be given in the following:

(1) Pump mode ($P_{in} < P_{out} < P_c$): The fluid emerges from the chamber due to the high chamber pressure P_c The intake element functions as a nozzle and the outflow element behaves like a diffuser.

$$-Q_1 + Q_2 = 2\pi f \cdot V_m \sin(2\pi f \cdot t) \tag{12a}$$

$$P_c = P_{out} + \frac{\rho}{2{A_t}^2} K_d^t Q_2^2 \tag{12b}$$

$$P_c = P_{in} + \frac{\rho}{2{A_t}^2} K_n^t Q_1^2 \tag{12c}$$

(2) Supply mode ($P_c < P_{in} < P_{out}$): The fluid is forced to flow into the chamber. Comparing with the pump mode, the functions of the intake and outflow elements are reversed.

$$Q_1 - Q_2 = 2\pi f \cdot V_m\ \sin(2\pi f \cdot t) \tag{13a}$$

$$P_c = P_{out} - \frac{\rho}{2{A_t}^2} K_n^t Q_2^2 \tag{13b}$$

$$P_c = P_{in} - \frac{\rho}{2{A_t}^2} K_d^t Q_1^2 \tag{13c}$$

(3) Transition mode ($P_{in} < P_c < P_{out}$): In this case, the fluid outside the outlet flows into the chamber and the outflow element works as a nozzle. In the mean time, the fluid inside the chamber flows out though the intake element, which also works as a nozzle.

$$-Q_1 - Q_2 = 2\pi f \cdot V_m \sin(2\pi f \cdot t) \tag{14a}$$

$$P_c = P_{out} - \frac{\rho}{2{A_t}^2} K_n^t Q_2^2 \tag{14b}$$

$$P_c = P_{in} + \frac{\rho}{2{A_t}^2} K_n^t Q_1^2 \tag{14c}$$

In the above, K_n^t and K_d^t denote the total loss coefficients of the nozzle and the diffuser, respectively, and V_m is one half of the maximum volume swept by the membrane. It is noted that the flow rates Q_1 and Q_2 are regarded as positive when they are in the direction of x-axis, i.e., in the direction from the left (inlet) to the right (outlet). The above equations can be solved to find Q_1, Q_2 and P_c if the total loss coefficients K_d^t and K_n^t are known.

The pressure loss across a nozzle or a diffuser consists of three parts. The major part is that due to the flow in the nozzle/diffuser itself. Other losses result from the sudden contraction at the entrance as well as the sudden expansion at the exit. The total loss coefficients can be expressed as [23]

$$K_d^t = K_{d,en} + K_d + \frac{A_t}{A_L} K_{d,ex} \tag{15a}$$

$$K_n^t = \left(\frac{A_t}{A_L}\right)^2 K_{n,en} + K_n + K_{n,ex} \tag{15b}$$

where A_t/A_L is the area ratio of the two ends of the nozzle/diffuser with A_t being the smaller one and A_L the larger one. For sharp-edge entrances, as in the present study, $K_{d,en} = K_{n,en} = 0.4$ and for exits, $K_{d,ex} = K_{n,ex} = 1$ regardless of the shape of the exit region [24]. The major loss coefficients, in general, depend upon the Reynolds number, or the flow rate. To simplify the problem, both K_d and K_n are assumed to be a function of one half of the instantaneous flow rate displaced by the membrane:

$$K_d(t) = K_d(Q(t) = \pi f V_m |\sin(2\pi f t)|) \tag{16a}$$

$$K_n(t) = K_n(Q(t) = \pi f V_m |\sin(2\pi f t)|) \tag{16b}$$

Three-dimensional simulations have been conducted to find the correlation between the loss coefficients and the flow rate. The geometry of the nozzle/diffuser element is the same as that used in the present micropump. The results (model A) are shown in Fig. 5. It is not surprised that the total loss coefficient for the nozzle K_n^t is greater than the total loss coefficient for the diffuser K_d^t. The relationships can be expressed as

$$K_d^t = 1.315 \times 10^{-7} Q^{-0.921} + 0.5981 \tag{17a}$$

$$K_n^t = 1.173 \times 10^{-6} Q^{-0.8112} + 1.204 \tag{17b}$$

In determination of the above correlations, three levels of grid with 15,000, 33,600, and 53,760 cells were tested. It was revealed that only minor differences were detected among the results for different grids.

A model was proposed by Yang et al. [25] to correlate the pressure loss and the Reynolds number for the flow through a micronozzle/diffuser. Employing this model leads to the following correlations:

$$K_d^t = 1.5838 \times 10^{-8} Q^{-0.9995} + 0.602 \tag{18a}$$

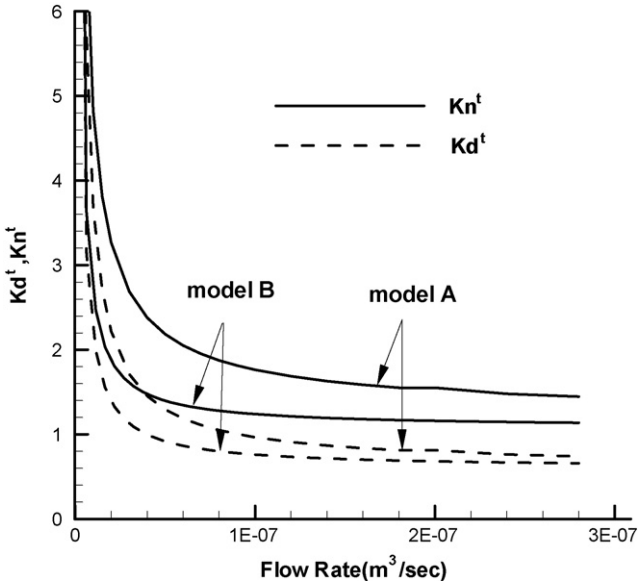

Fig. 5. Variation of the loss coefficients against the flow rate for the nozzle and diffuser for the two models.

$$K_n^t = 1.5838 \times 10^{-8} Q^{-0.998} + 1.081 \tag{18b}$$

They are also shown in Fig. 5 as model B. The correlations for the two models are valid for Reynolds numbers less than 400. The flows in the present micropump fall in this range.

4. Pumping efficiency

The real efficiency of the membrane pump is defined by

$$\eta_R = \frac{\Delta Q}{2V_m} \tag{19}$$

Here ΔQ is the net volume of the flow through the pump in one period T and $2V_m$ is the volume swept by the membrane from the top dead center (TDC) to the bottom dead center (BDC). The change rate of volume of this harmonic motion can be written as

$$\frac{dV}{dt} = 2\pi f V_m \sin(2\pi f t) \tag{20}$$

The net flow volume through the pump in one period T is obtained from

$$\Delta Q = \frac{1}{2}\int_0^T (Q_2(t) - Q_1(t))\, dt \tag{21}$$

where Q_1 is the flow rate into the chamber at the inlet and Q_2 that out of the chamber at the outlet. We assume that Q_1 varies in a harmonic manner similar to the membrane:

$$Q_1(t) = Q_m \sin(2\pi f t) \tag{22}$$

Then

$$\Delta Q = \frac{Q_m}{2}\int_0^T (\beta(t) - 1)\, \sin(2\pi f t)\, dt \tag{23}$$

where β is the ratio of the outlet flux to the inlet flux.

$$\beta(t) = \frac{Q_2(t)}{Q_1(t)} \tag{24}$$

The change rate of the chamber volume dV/dt is equal to $2Q_1$ approximately. Thus,

$$V_m = \frac{Q_m}{\pi f} \tag{25}$$

Substituting Eqs. (23) and (25) into Eq. (19) yields an approximate pumping efficiency denoted by η_1:

$$\eta_1 = \frac{\pi f}{4}\int_0^T (\beta(t)-1)\ \sin(2\pi f t)\,\mathrm{d}t \tag{26}$$

The formulation can be further simplified if the flow rate can be represented by some constants. It was seen that the variation of the ratio is considerably flat in either the pumping stage or the supply stage except near the transition region. Two average flow ratios corresponding to the pumping stage and the supply stage are defined as

$$\beta_\mathrm{p} = \frac{5}{2T}\int_{T/20}^{9T/20} \beta(t)\ \mathrm{d}t \tag{27a}$$

$$\beta_\mathrm{s} = \frac{5}{2T}\int_{11T/20}^{19T/20} \beta(t)\,\mathrm{d}t \tag{27b}$$

The reason for the integration over $2T/5$ only is to avoid the transition region, which will become clearer in the case tests shown later. Eq. (26) can then be integrated to yield:

$$\eta_2 = \frac{\pi f}{4}\left[\int_0^{T/2}(\beta_\mathrm{p}-1)\ \sin(2\pi f t)\,\mathrm{d}t + \int_{T/2}^{T}(\beta_\mathrm{s}-1)\sin(2\pi f t)\,\mathrm{d}t\right]$$
$$= \frac{1}{4}(\beta_\mathrm{p}-\beta_\mathrm{s}) \tag{28}$$

This pumping efficiency only depends on the constant ratios β_p and β_s. It is noted that in general, $\beta_\mathrm{p} > 1$ and $\beta_\mathrm{s} < 1$.

Another simplified form of pumping efficiency can be derived from the following assumptions for Q_1 and Q_2 in the first half period:

$$Q_1(t) = Q_{\mathrm{m}1}\sin(2\pi f t) \tag{29a}$$

$$Q_2(t) = Q_{\mathrm{m}2}\ \sin(2\pi f t) \tag{29b}$$

Thus,

$$\Delta Q = \int_0^{T/2}(Q_2(t)-Q_1(t))\ \mathrm{d}t = \frac{1}{\pi f}(Q_{\mathrm{m}2}-Q_{\mathrm{m}1}) \tag{30}$$

Since

$$V_\mathrm{m} = \frac{1}{2\pi f}(Q_{\mathrm{m}1}+Q_{\mathrm{m}2}), \tag{31}$$

The pumping efficiency can be given by

$$\eta_3 = \frac{Q_{\mathrm{m}2}-Q_{\mathrm{m}1}}{Q_{\mathrm{m}2}+Q_{\mathrm{m}1}} \tag{32}$$

Let

$$\beta_\mathrm{p} = \frac{Q_{\mathrm{m}2}}{Q_{\mathrm{m}1}} \tag{33}$$

It is obtained

$$\eta_3 = \frac{\beta_\mathrm{p}-1}{\beta_\mathrm{p}+1} \tag{34}$$

In the multidimensional and lumped-system analyses, β_p is estimated using Eq. (27a). It is interesting to notice that the same expression for the pumping efficiency η_3 can be found in the study of Olsson et al. [4] by replacing β_p by the square root of efficiency of the nozzle/diffuser $\eta_\mathrm{nd}^{1/2}$ where

$$\eta_\mathrm{nd} = \frac{K_\mathrm{n}}{K_\mathrm{d}} \tag{35}$$

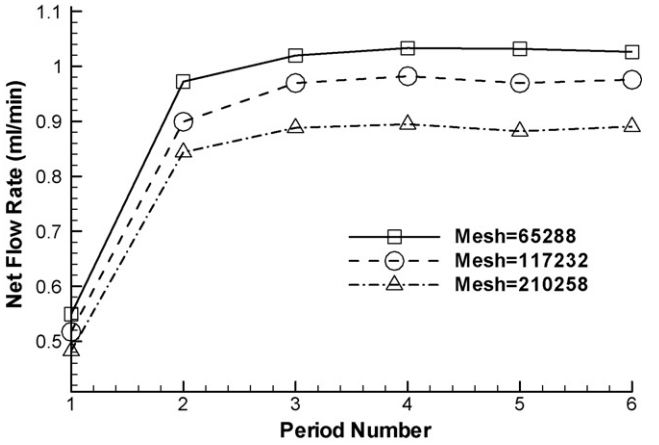

Fig. 6. The net flow rates in each period for different levels of grid for the case $P_\mathrm{b} = 0$.

K_n and K_d are loss coefficients of the nozzle and the diffuser, respectively. It can be noticed from Eq. (11) that for a constant pressure loss across a nozzle/diffuser, $K^{1/2} \sim 1/Q$.

5. Results

The settings of the geometry of the micropump are given in Fig. 1. It is assumed that the membrane reciprocates in a harmonic motion with a frequency of 2200 Hz. The maximum amplitude of the vibration is 1.0 μm. The large ratio of the chamber height to the vibration amplitude justifies the use of moving velocity instead of moving surface as the boundary condition. Zero pressure is specified at the inlet and various back pressures P_b, ranging from 0 to 5900 Pa, are set at the outlet. Calculations were undertaken for a

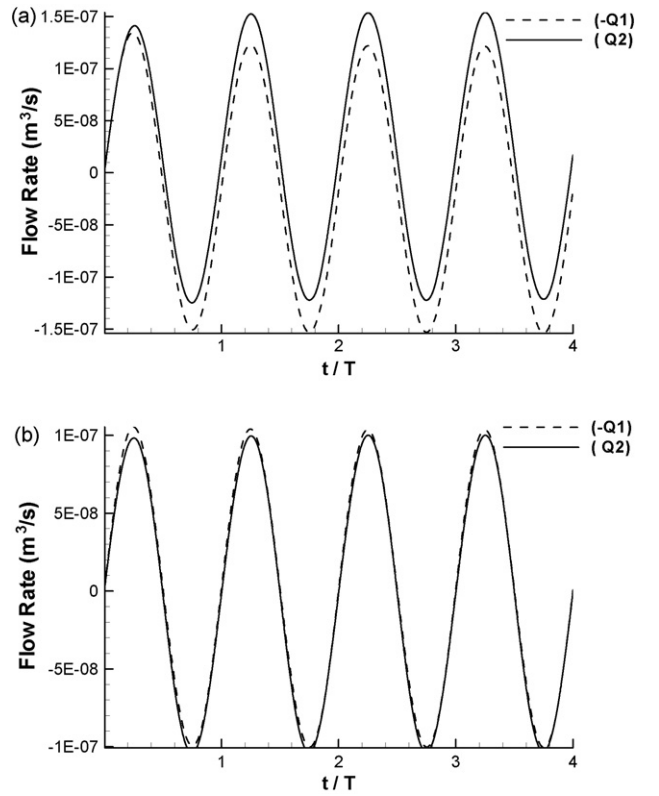

Fig. 7. Variation of the flow rates at the inlet (Q_1) and outlet (Q_2) for (a) $P_\mathrm{b} = 0$ and (b) $P_\mathrm{b} = 5310$ Pa.

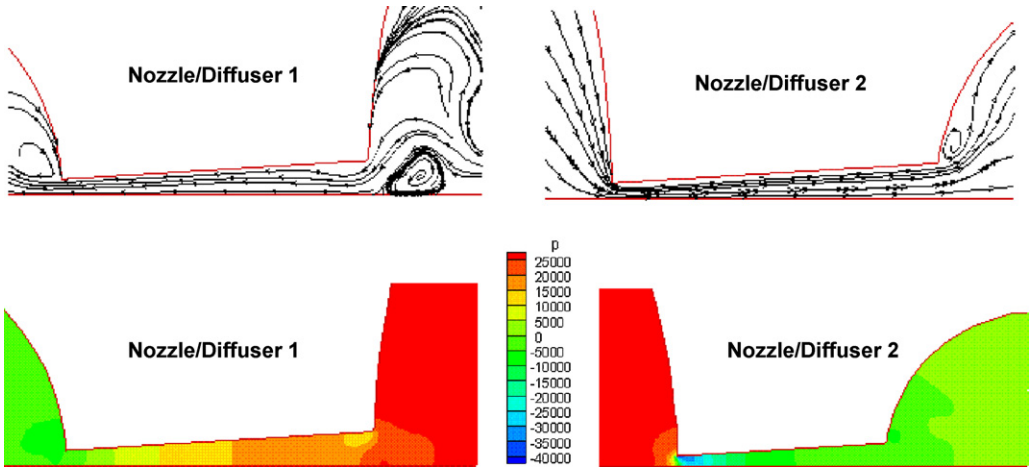

Fig. 8. The plots of streamlines and pressure contours in the two nozzle/diffuser regions at $t = T/4$.

number of periods. The net flow rates averaged over each period for different levels of grid are given in Fig. 6 for the case with $P_b = 0$. It can be observed that it takes at least three periods for the flow to become fully periodic.

The pumping effect caused by the valveless micropump becomes clear by viewing the variation of the flow rates $-Q_1$ (negative value of Q_1) and Q_2, as shown in Fig. 7. For the case $P_b = 0$ the flow rate at the outlet Q_2 is higher than the flow rate at the inlet $-Q_1$ in the first half of a period (the pumping stage) due to the diffuser function of the element connecting the outlet chamber and the nozzle function of the element connecting the inlet chamber. In the second half of the period, the absolute value of Q_2 becomes lower than that of Q_1 because the flow direction is reversed (the supply stage). The flow rate Q_2 can be approximately expressed by a sinusoidal function $a + b \sin \omega t$ and the flow rate $-Q_1$ by $-a + b \sin \omega t$. The constant a represents the net flow rate. For the case $P_b = 5310$ Pa the variations of the flow rates $-Q_1$ and Q_2 are very close to each other and the net flow rate, or the constant a, approaches zero.

To illustrate the flow field, the plots of streamlines and pressure contours in the two nozzle/diffuser regions at $t = T/4$ and $3T/4$ are shown in Figs. 8 and 9, respectively. At $t = T/4$ in the pumping stage, the flow is directed from the main chamber toward the inlet and the outlet chambers. The discharge element on the left functions as a nozzle and that on the right as a diffuser. The pressure decreases gradually is the nozzle whereas the pressure drops sharply at the entrance of the diffuser and then recovers gradually. It can be seen that there exists a recirculation zone near the entrance corner in the nozzle and another recirculation zone before the fluid enters the nozzle. The former is caused by the sharp entrance while the latter is due to the fact that as seen in Fig. 9 for $t = 3T/4$, the recirculation formed by the flow emerging from the nozzle/diffuse element in the supply stage persists and moves down toward the central region during the pump stage. The recirculating flow leads to a low pressure region at the entrance of the nozzle and, thus, causes additional losses. The flow type is reversed in the supply stage at $t = 3T/4$. It can be detected that both the velocity and pressure fields in Fig. 9 are very similar to those in Fig. 8 except that the roles of the two nozzle/diffuser elements are interchanged.

The multidimensional solution procedure is validated by comparing the predicted net flow rates with the measurements of Olsson et al. [7], as shown in Fig. 10. The calculations were performed using the parabolic, trapezoidal, and blending profiles, as given by Eq. (7). As expected, the net flow rates decrease when the back pressure increases. In general, the flow rates are overpredicted by using the trapezoidal profile, especially for sufficiently large P_b, and underpredicted when the parabolic profile is employed. The higher flow rate obtained by using the trapezoidal profile is due to its larger volume displacement. The strategy in the blending profile is to use the trapezoidal profile at $P_b = 0$, the parabolic profile

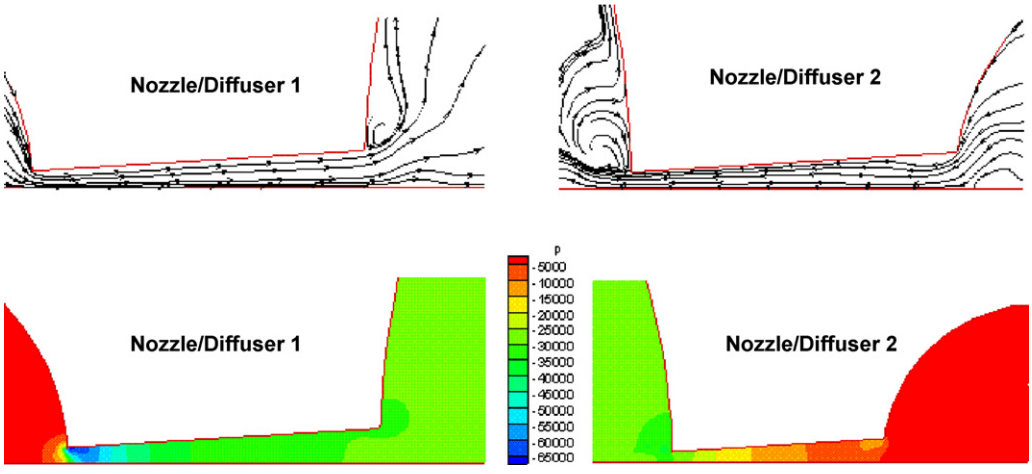

Fig. 9. The plots of streamlines and pressure contours in the two nozzle/diffuser regions at $t = 3T/4$.

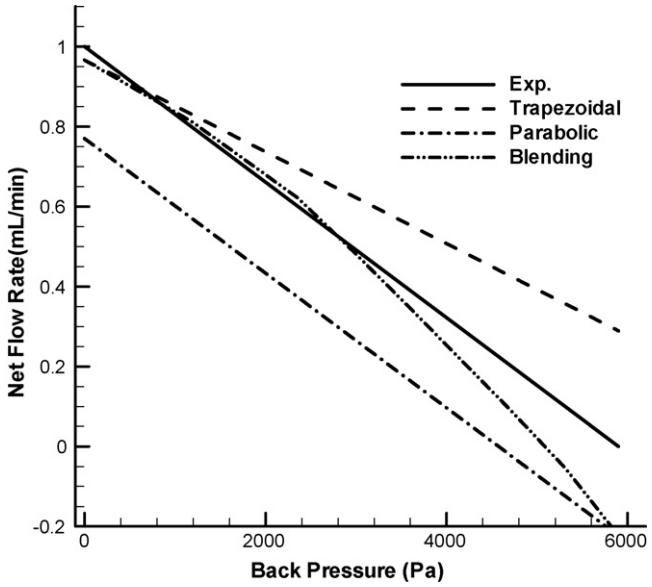

Fig. 10. Comparison of predicted net flow rates using different membrane profiles with measurements at various back pressures.

at P_b = 5900 Pa, and a linear combination of the two in between. As seen from the figure, the resulting flow rates become much closer to the experiment data.

Calculations were conducted using grids with 65,288, 117,232 and 210,258 cells. The computational time step is $T/400$ for the two coarse meshes and is reduced to $T/800$ for the finest mesh to suppress instabilities which may lead to divergence of the solution procedure. As shown in Fig. 6, moderate differences in the results for different meshes could be detected. No further efforts were taken to find fully grid-independent solutions due to too much computer resources required. However, it can be concluded from the above tests that with a suitable membrane profile accurate results can be obtained. The multidimensional results serve as benchmark solutions for the lumped-system analysis to compare. Two different expressions have been described to correlate the loss coefficients and the flow rates for the nozzle/diffuser element. Eqs. (17a) and (17b), termed model A, were obtained from the multidimensional simulation for the nozzle/diffuser configuration considered in the present study. Eqs. (18a) and (18b), termed as model B, were adopted from the study of Yang et al. [25]. The resulting flow rates at the outlet (Q_2) in one period are presented in Fig. 11 for back pressures P_b = 0 and 5310 Pa. The first half of the period corresponds to the pumping stage and the second half the supply stage. The positive Q_2 indicates the flow out of the outlet. It is seen that the curves by the models follow the multidimensional results closely for the case with P_b = 0. It can be detected that the values of Q_2 at t/T = 0 and 1 are not zero in the multidimensional calculations due to the inertial effect of the flow at the end of the supply mode. This effect is not accounted for in the lump models. The differences between the multidimensional simulation and the model results increase with increasing back pressure. There appears non-smoothness in the variation of Q_2 obtained by the lumped-system analyses in the transition region between the pumping stage and the supply stage. This is also ascribable to the inertial effect not taken into account. It is noted that the driving momentum of the membrane is low in the transition stage and, thus, the inertial effect becomes more prominent. When a pressure difference exists between the inlet and the outlet, the variation of the pressure in the chamber becomes not so regular, resulting in the kinks seen in Fig. 11b. Comparing with the multidimensional

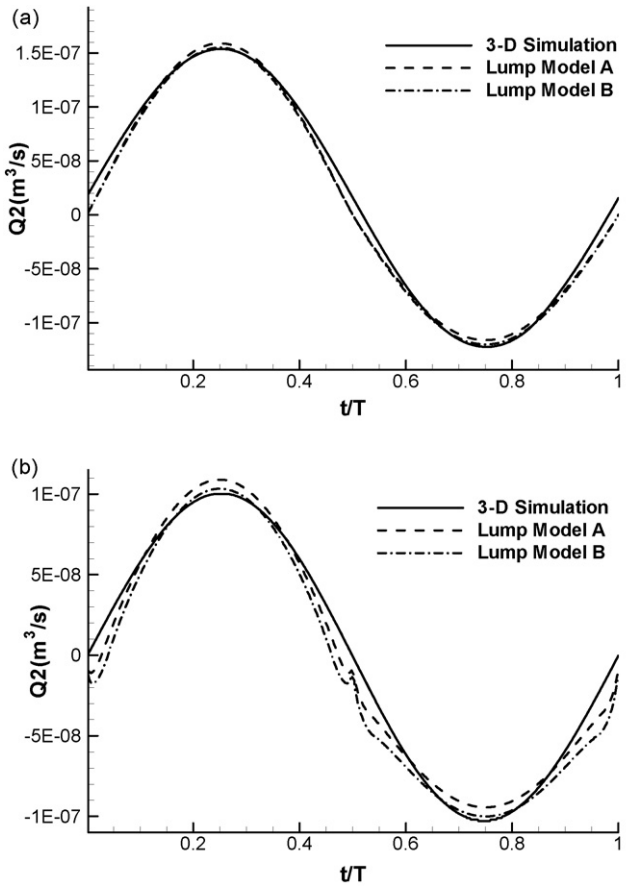

Fig. 11. Variation of the flow rates at the outlet in one period predicted by the 3D simulation and the two lump models for (a) P_b = 0 and (b) P_b = 5310 Pa.

simulation, closer agreement is obtained by the model A. This is evident in Fig. 12 by examining the real efficiency η_R.

The variation of the flow rate ratio $\beta(=Q_2/Q_1)$ is shown in Fig. 13. Generally, the value of β is greater than 1 in the first half of the period (the pumping stage) and less than 1 in the second half (the supply stage) in the case P_b = 0, implying a net flow from the inlet to

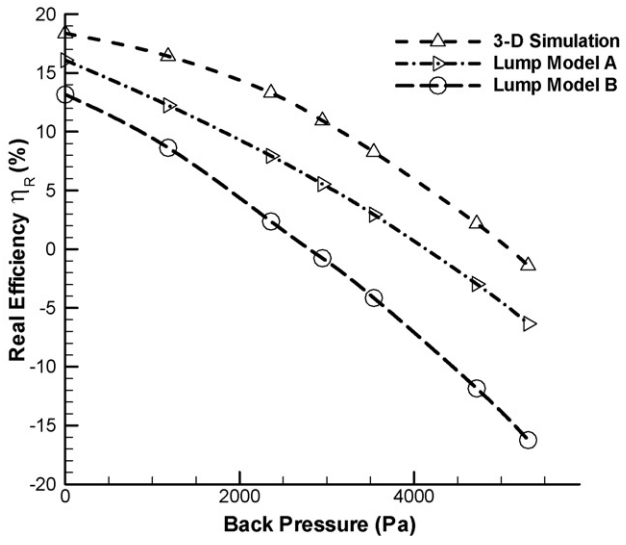

Fig. 12. Comparison of the real efficiencies predicted by the 3D simulation and the two lump models.

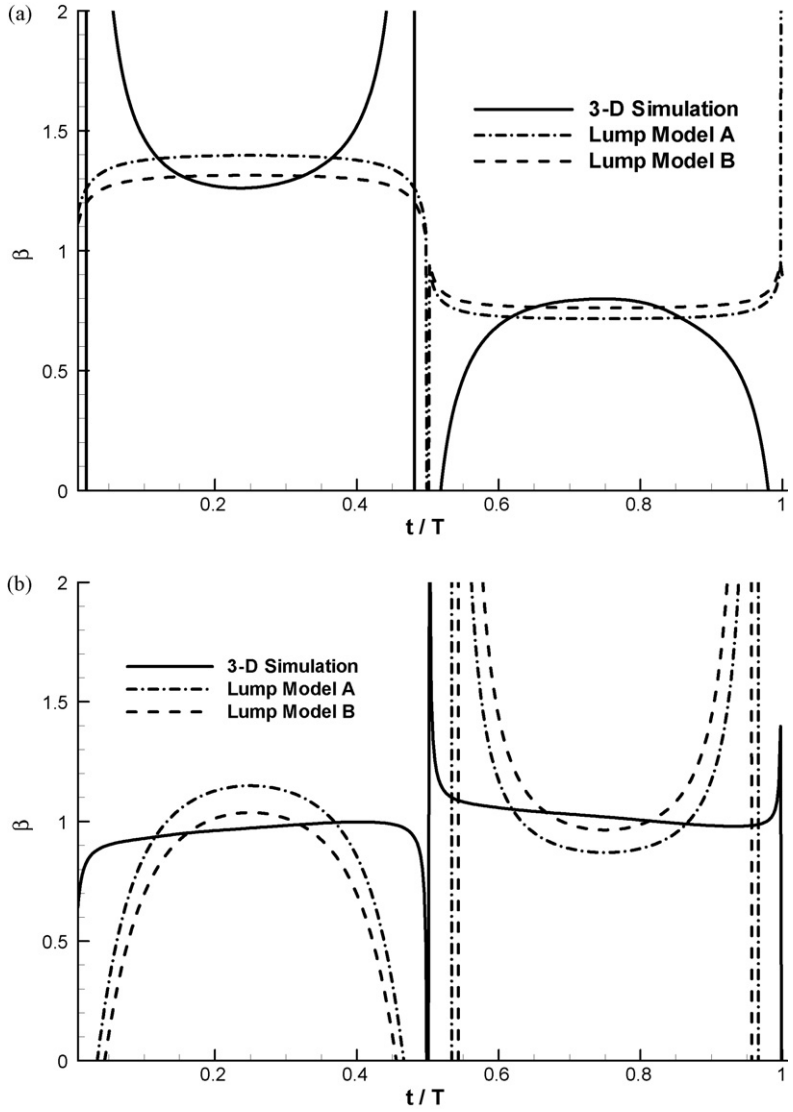

Fig. 13. Comparison of the flow rate ratios β in one period obtained by the 3D simulation and the two lump models for (a) $P_b = 0$ and (b) $P_b = 5310$ Pa.

the outlet. In the pumping stage, the curve obtained by the multidimensional simulation is of concave type and those by the two lump models are of convex type. The curve types for the multidimensional simulation and the models are interchanged in the supply stage. The different types of curves are believed to be caused by the inertial effect being absent in the lump models. With $P_b = 5310$ Pa, there is almost no net flow. This is reflected in the fact that the values of β become close to one, as seen in Fig. 13b. In contrast to the case $P_b = 0$, the curves for the multidimensional simulation and the two models are of the same type.

It can be seen from the above figure that the value of β may approach positive or negative infinity and completely different characteristics in β appear in the multidimensional calculations and the model predictions in the transition region. This is the reason why the two mean flow ratios β_p and β_s, appearing in the simplified formulations for pumping efficiency (η_2 and η_3), are estimated by averaging over $4T/5$ only in the corresponding first and second halves of a period to avoid the transition region as done in Eqs. (27a) and (27b). The variations of β_p and β_s for different back pressures are displayed in Fig. 14. Obviously, by using the model A the agreement with the multidimensional simulation is closer. As shown in Fig. 15, the approximate efficiencies η_2 and η_3 obtained

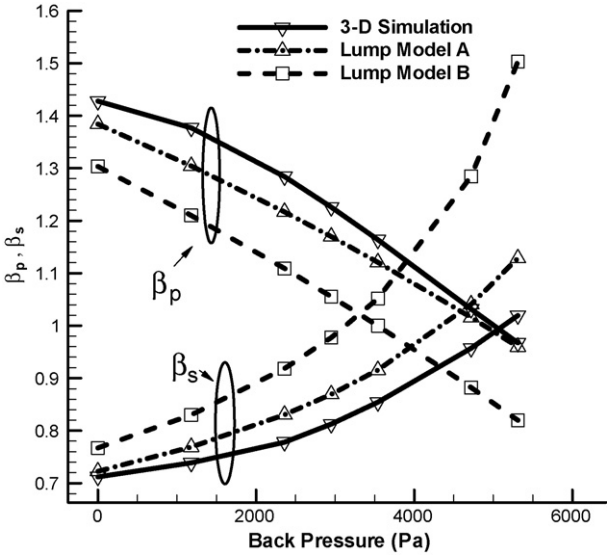

Fig. 14. Comparison of the flow rate ratios β_p and β_s obtained by the 3D simulation and the two lump models.

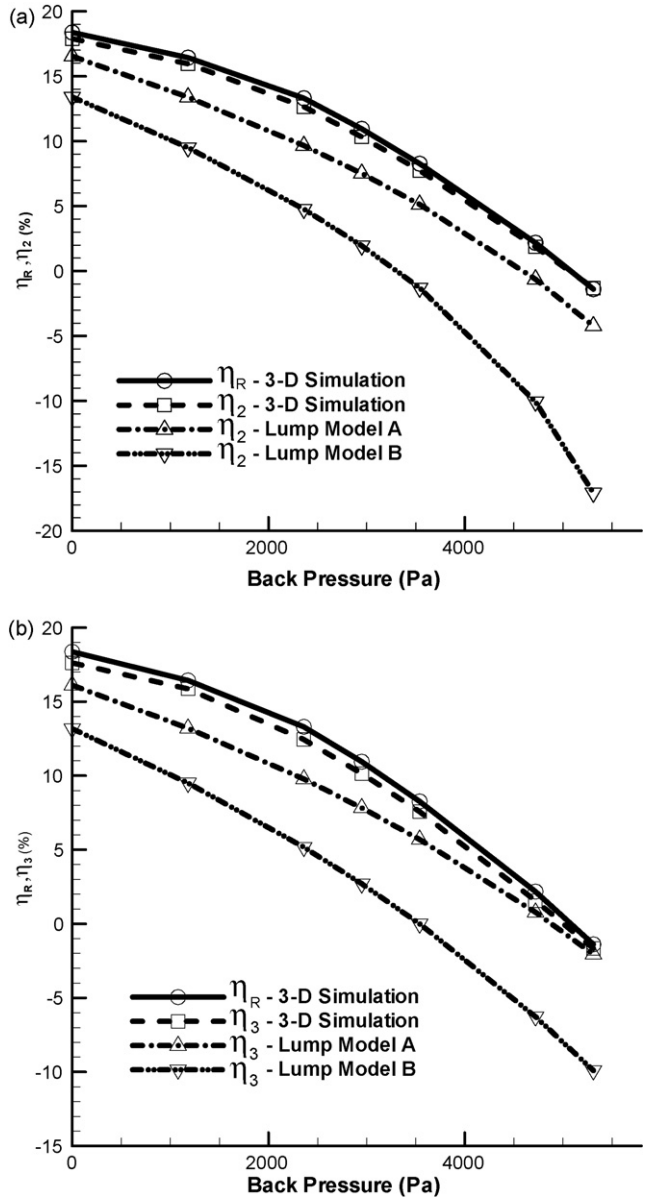

Fig. 15. Comparison of the predicted efficiencies η_2 and η_3 by the 3D simulation and the two lump models.

from the multidimensional simulation are only marginally lower than the real efficiencies η_R. The under-estimate of the approximate efficiencies by the lumped-system analysis is considerable, with the model A being the better. The comparison between the two approximate efficiencies indicates that η_3 is slightly better at high back pressures. It is of interest to notice that comparing with the real efficiencies η_R obtained from the lumped models shown in Fig. 12, the approximate efficiencies η_2 and η_3 of the lump models are even closer to the η_R obtained by the multidimensional calculations. This is ascribed to the smart ignorance of the transition regions in calculating β_p and β_s.

6. Conclusions

A CFD solution method has been developed to examine the unsteady flow field prevailing in the valveless micropump. The conservative equations are solved using the finite volume approach within the frame of unstructured grid. The pressure boundary conditions specified at the inlet and outlet openings are tackled using a mass conservation treatment, which is more appropriate for unsteady flow calculations. The vibration of the membrane is modeled by a reciprocating velocity boundary condition derived from a harmonic motion. The deflection of the membrane during vibration is assumed to be of a shape blending the parabolic and trapezoidal curve profiles. The different characteristics of the nozzle and the diffuser results in a net pumping flow from the inlet to the outlet. The agreement in the net flow rate between predictions and measurements is satisfactory.

The performance of the micropump has also been analyzed using the lumped-system method. In the lump model the relations between the loss coefficients and the flow rates for the nozzle and the diffuser are expressed in two descriptions. One of the two correlations is obtained by the multidimensional simulation for the considered nozzle/diffuser element. With this specially tailored correlation, a better agreement with the CFD calculations has been achieved.

The pumping performance depends upon the ratio of the outlet flow rate to the inlet flow rate. Comparing with the multidimensional calculations, the variation of the flow rate ratio is quite different in the lumped-system analysis, especially in the transition region between the pumping stage and the supply stage, due to the inertial effect not taken into account in this simple method. The pumping efficiency of the pump has been formulated in two simplified expressions which are functions of the mean ratios of the two flow rates. In the averaging process to determine the mean ratios in the pumping and supply stages, the transition regions are ignored to reduce the influence of the inertial effect not accounted for in the lumped-system analysis. This simply results in better agreement with the CFD calculations in terms of the pumping efficiency.

References

[1] N.-T. Nguyen, X. Huang, T.K. Chuan, MEMS-micropumps: a review, ASME J. Fluids Eng. 124 (2002) 384–392.
[2] D.J. Laser, J.G. Santiago, A review of micropump, J. Micromech. Microeng. 14 (2004) R35–R64.
[3] P. Woias, Micropumps—past, progress and future prospects, Sens. Actuator B 105 (2005) 28–38.
[4] E. Stemme, G. Stemme, A valveless diffuser/nozzle-based fluid pump, Sens. Actuator A 39 (1993) 159–167.
[5] T. Gerlach, H. Wurmus, Working principle and performance of the dynamic micropump, Sens. Actuator A 50 (1995) 135–140.
[6] A. Olsson, G. Stemme, E. Stemme, A valve-less planar fluid pump with two pump chambers, Sens. Actuator A 46–47 (1995) 549–556.
[7] A. Olsson, O. Larsson, J. Holm, L. Lundbladh, O. Ohman, G. Stemme, Valve-less diffuser micropumps fabricated using thermoplastic replication, Sens. Actuator A 64 (1998) 63–68.
[8] A. Ullmann, The piezoelectric valve-less pump-performance enhancement analysis, Sens. Actuator A 69 (1998) 97–105.
[9] A. Olsson, G. Stemme, E. Stemme, A numerical design study of the valveless diffuser pump using a lumped-mass model, J. Micromech. Microeng. 9 (1999) 34–44.
[10] L.S. Pan, T.Y. Ng, G.R. Liu, K.Y. Lam, T.Y. Jiang, Analytical solutions for the dynamic analysis of a valveless micropump—a fluid–membrane coupling study, Sens. Actuator A 93 (2001) 173–181.
[11] L.S. Pan, T.Y. Ng, X.H. Wu, H.P. Lee, Analysis of valveless micropumps with inertial effects, J. Micromech. Microeng. 13 (2003) 390–399.
[12] N.-T. Nguyen, X. Huang, Numerical simulation of pulse-width-modulated micropumps with diffuser/nozzle elements, in: Proceedings of the International Conference on Modeling Simulation of Microsystems MSM2000, Santiego, CA, 2000, pp. 636–639.
[13] K.-S. Yang, I.-Y. Chen, C.-C. Wang, Performance of nozzle/diffuser micro-pumps subject to parallel and series combinations, Chem. Eng. Technol. 29 (6) (2006) 703–710.
[14] B. Fan, G. Song, F. Hussain, Simulation of a piezoelectrically actuated valveless micropump, Smart Mater. Struct. 14 (2005) 400–405.
[15] Q. Yao, D. Xu, L.S. Pan, A.L.M. Teo, W.M. Ho, V.S.P. Lee, M. Shabbir, CFD simulation of flows in valveless micropumps, Eng. Appl. Comput. Fluid Mech. 1 (3) (2007) 181–188.

[16] J. Jeong, C.N. Kim, A numerical simulation on diffuser-nozzle based piezoelectric micropumps with two different numerical models, Int. J. Numer. Method Fluids 53 (2007) 561–571.
[17] Y.-Y. Tsui, Y.-F. Pan, A pressure-correction method for incompressible flows using unstructured meshes, Numer. Heat Transf. B 49 (2006) 43–65.
[18] Y.-Y. Tsui, T.-C. Wu, A pressure-based unstructured-grid algorithm using high-resolution schemes for all-speed flows, Numer. Heat Transf. B 53 (2008) 75–96.
[19] R.I. Issa, Solution of the implicitly discretised fluid flow equation by operator-splitting, J. Comput. Phys. 62 (1985) 40–65.
[20] Y.-Y. Tsui, S.-P. Jung, Analysis of the flow in grooved pumps with specified pressure boundary conditions, Vacuum 81 (2006) 401–410.
[21] Y.-Y. Tsui, C.-Y. Lu, A study of the recirculating flow in planar, symmetrical branching channels, Int. J. Numer. Method Fluids 50 (2006) 235–253.
[22] S.P. Timoshenko, S. Woinowsky-Krieger, Theory of Plates and Shells, 2nd edn., McGraw-Hill, New York, 1959.
[23] A. Olsson, G. Stemme, E. Stemme, Diffuser-element design investigation for valve-less pumps, Sens. Actuator A 57 (1996) 137–143.
[24] A. Olsson, G. Stemme, E. Stemme, Numerical and experimental studies of flat-walled diffuser elements for valve-less micropumps, Sens. Actuator A 84 (2000) 165–175.
[25] K.-S. Yang, I.-Y. Chen, B.-Y. Shew, C.-C. Wang, Investigation of the flow characteristics within a micronozzle/diffuser, J. Micromech. Microeng. 14 (2004) 26–31.

Biographies

Yeng-Yung Tsui received MSc from University of Tennessee Space Institute, U.S.A in 1981 and PhD from Imperial College of Science and Technology, U.K., in 1987. He joined the Department of Mechanical Engineering, National Chiao Tung University, Taiwan, ROC, since then and is currently a professor of the department. His major research interests lie in the computational fluid dynamics. Recently, he was involved in the studies of molecular pumps, mixers with agitators, two-fluid flows, and microfluid flows.

Shiue-Lin Lu received his BSc from Tamkang University in 2005 and MSc from National Chiao Tung University, Taiwan, ROC, in 2007. He is currently in the military service. His research during the graduate study was concerned with the analysis of the flow in micropumps.